Journal of Power Sources 195 (2010) 6598–6610

Contents lists available at ScienceDirect

Journal of Power Sources

journal homepage: www.elsevier.com/locate/jpowsour

Combined micro-scale and macro-scale modeling of the composite electrode of a solid oxide fuel cell

Daifen Chen, Wuxi Bi, Wei Kong, Zijing Lin*

Hefei National Laboratory for Physical Sciences at Microscale and Department of Physics, University of Science and Technology of China, Hefei 230026, China

ARTICLE INFO

Article history:
Received 20 February 2010
Received in revised form 20 April 2010
Accepted 20 April 2010
Available online 27 April 2010

Keywords:
Solid oxide fuel cell
Composite electrode
Percolation theory
Multi-physics modeling
Electrochemical reaction
Activation overpotential

ABSTRACT

The design of a cathode inter-layer is important to the high performance of a solid oxide fuel cell (SOFC). In this paper, the processes of electrochemical reactions, electronic and ionic conductions and gas transports in an SOFC are discussed in detail. An analysis shows that the current conduction and electrochemical processes can be replicated by an equivalent circuit model. A corresponding macro-scale model using the Butler–Volmer equation for electrochemical reactions, Ohm's law for current conduction and the Dusty-gas model for gas transport is described. A percolation theory based micro-model is used to obtain the effective electrode properties in the macro-model from the microstructure parameters of the porous electrode. Experimental *I–V* relations can be accurately accounted for by the proposed theory. The macro- and micro-models are then combined to systematically examine the effects of various parameters on the performance of a composite cathode inter-layer. The examined parameters include the thickness, effective electronic and ionic conductivities, exchange current density, operating temperature, output current density, electrode- and electrolyte-particle radii, composition and porosity of the cathode inter-layer. The comprehensive study shows conclusively that a cathode inter-layer thickness in a range of 10–20 μm is optimal for all practical material choices and microstructure designs.

1. Introduction

To achieve high fuel cell performance, engineers are exploring increasingly sophisticated structures for solid oxide fuel cell (SOFC) electrodes. One common approach is to use functional graded porous composite electrodes, and extensive efforts have been devoted to examining the effects of various structural and material parameters on cell performance [1–5]. A typical composite electrode is a mixture of electrode-particles, such as Ni or lanthanum-doped strontium manganate (LSM), and electrolyte-particles, such as yttria-stabilized zirconia (YSZ) [1,6]. It provides parallel paths for oxygen ions (through YSZ), electrons (through Ni and LSM), and gaseous species (through the pores) [7,8].

Fig. 1 shows a typical anode-supported SOFC, which consists of five distinct layers: (a) a porous Ni + YSZ anode support layer with relatively large Ni- and YSZ-particles, (b) a porous Ni + YSZ anode inter-layer with fine Ni- and YSZ-particles, (c) a dense YSZ electrolyte layer, (d) a porous LSM + YSZ cathode inter-layer with fine LSM- and YSZ-particles, and (e) a porous LSM cathode current collector with relatively large LSM-particles. The composite nature of a porous electrode allows for a large number of triple-phase-boundaries (TPBs), in which three distinct transporting phases meet, i.e., LSM-YSZ-pores or Ni-YSZ-pores. On the cathode side, oxygen from a gas channel is transported through a porous cathode current collector to a cathode TPB (gas-LSM-YSZ). At the cathode TPB, an electrochemical reaction occurs between oxygen and electrons, which come from an external circuit through the electronic conducting phase of the cathode. The product (O^{2-}) is then transported to the anode TPB through an ionic conducting phase within the cathode inter-layer, electrolyte and anode inter-layer. At the anodic TPB, fuel (e.g., H_2) from the channel is transported through the porous anode to the anode TPB and reacts with the oxygen ions. The product H_2O is transported back to the fuel channel through the porous anode structure and e^- are conducted to the external circuit through the electronic conductive phase of the anode.

The above-described transports of gas species, electrons and ions and electrochemical reactions may cause various types of polarizations. Concentration overpotential is caused by the transporting resistance of gaseous species through a porous structure. Ohmic polarization is caused by conducting resistances of electrons and ions within the composite electrodes and a dense electrolyte [9,10]. Activation overpotential is caused by the energy barriers for the electrochemical reaction at TPBs [7,11,12]. As the state of the art of composite electrodes becomes increasingly sophisticated [13,14], there is an increasing need to understand the detailed chemical and physical processes within composite electrodes and develop a quantitative theory to predict the influence of microstructures on fuel cell performance. Applying this knowledge

* Corresponding author. Tel.: +86 551 3606345; fax: +86 551 3606348.
E-mail address: zjlin@ustc.edu.cn (Z. Lin).

0378-7753/$ – see front matter © 2010 Elsevier B.V. All rights reserved.
doi:10.1016/j.jpowsour.2010.04.065

Nomenclature

B_0	flow permeability, m^2
$D^{eff}_{\alpha\beta}$	effective binary diffusivity, $m^2\ s^{-1}$
$D^{eff}_{\alpha K}$	effective Knudsen diffusivity for gas species α, $m^2\ s^{-1}$
E_{H_2}	activation energy for H_2 oxidation, $J\ mol^{-1}$
E_{O_2}	activation energy for O_2 reduction, $J\ mol^{-1}$
E_0	Nernst potential, V
E^{eq}	equilibrium electric potential difference at electrochemical reaction interface, V
F	Faraday constant, $C\ mol^{-1}$
j_{TPB}	charge transfer rate per unit TPB length, $A\ m^{-1}$
j_0	local exchange transfer current per unit TPB length, $A\ m^{-1}$
$j_{0,ref}$	parameter in the expression of j_0, $A\ m^{-1}$
i_{op}	output current density, $A\ m^{-2}$
i_e	local electronic current density, $A\ m^{-2}$
i_i	local ionic current density, $A\ m^{-2}$
$i^V_{e,i}$	volumetric charge transfer rate, $A\ m^{-3}$
$i^S_{e,i}$	charge transfer rate per unit dense electrolyte surface, $A\ m^{-2}$
L^c	cathode inter-layer thickness, m
M_α	molecular weight of gas species α, $kg\ mol^{-1}$
n^V_k	number of k-particles per unit volume
n^S_k	number of k-particles per unit dense electrolyte surface
N_α	molar flux of gas species α, $mol\ m^{-2}\ s^{-1}$
p	total gas pressure in electrode, atm
p^0_α	partial pressure of gas species α in gas channel, atm
p_α	partial pressure of gas species α in electrode, atm
P_k	percolation probability of k-particle
r_g	hydraulic pore radius, m
r_k	radius of k-particle, m
R	universal gas constant, $J\ mol^{-1}\ K^{-1}$
R_α	reaction rate of species α, $mol\ m^{-3}\ s^{-1}$
T	operating temperature, K
T_{ref}	reference temperature, K
ν_α	diffusion volume for gas species α, $m^3\ mol^{-1}$
V_{op}	output voltage, V
x_α	molar fraction of gas species α
$Z_{k,\ell}$	average number of contacts between a k-particle and ℓ-particles
$\bar{Z}$	overall average coordination number of all solid particles

Greek

α_f, β_r	the forward and reverse reaction symmetric factors
η	polarization, V
$\lambda^V_{TPB,eff}$	percolated TPB length per unit volume, m^{-2}
$\lambda^S_{TPB,eff}$	percolated TPB length per \dense electrolyte surface, m^{-1}
μ	viscosity, $kg\ m^{-1}\ s^{-1}$
μ_α	chemical potential of species α, J
ϕ_g	porosity
Φ_e	local electronic electric potential in electrode-phase, V
$\hat{\Phi}^a_e$	Φ_e in anode-phase shifted by a reference potential, V
$\hat{\Phi}^c_e$	Φ_e in cathode-phase shifted by a reference potential, V
Φ_i	local ionic electric potential in electrolyte-phase, V
$\hat{\Phi}_i$	Φ_i in electrolyte-phase shifted by a reference potential, V
ψ_k	volume fraction of k-particles in solid phase
ψ^t_k	threshold volume fraction of k-particles
σ^{eff}_{ed}	effective electronic conductivity, $S\ m^{-1}$
σ^{eff}_{el}	effective ionic conductivity, $S\ m^{-1}$
σ^0_k	electric conductivity of k-material in dense solid, $S\ m^{-1}$
τ	tortuosity of gas transport path
θ	contact angle between electrode- and electrolyte-particles

Superscripts and subscripts

a	anode
act	activation
c	cathode
con	concentration
cr	contact resistance
e	dense electrolyte
ed	electrode-particle
el	electrolyte-particle
ohm	ohmic

is important to the design, optimization, and fabrication of certain microstructure architectures as a means to achieve high fuel cell performance.

The task of understanding the relationship between electrode properties and microstructure seems to rest naturally on micro-scale models [15–20]. As an electrochemical reaction can only occur at sites where electrons, ions and chemical species coexist simultaneously, only those TPBs in which each of the three transportation phases belong to a percolated network can support the transport of relevant reactant species. These TPBs are defined as percolated TPBs and are important factors in determining cell performance. Because the percolation micro-model is generally regarded to be accurate and convenient in relating electrode properties with electrode microstructure through a coordination number [21,22], this work adopts such a micro-model [4] for estimating from the microstruc-

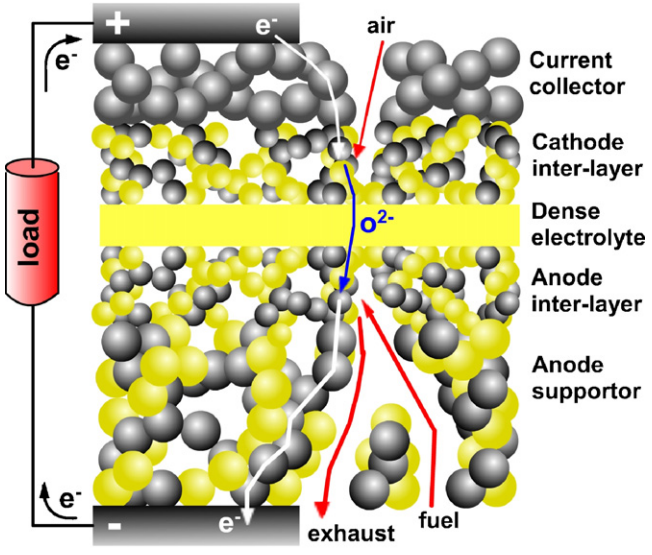

Fig. 1. Sketch of the physical processes in an anode-supported SOFC with functional graded electrodes. Dark particles represent electrode-particles and light particles represent electrolyte-particles.

ture the electrode properties, such as percolated TPB lengths per unit volume, percolated TPB lengths per unit dense electrolyte surface, effective electron and ion conductivities, hydraulic pore radius, and others. This micro-model not only satisfies the contact number conservation requirement [4,22], but also can be used to estimate the electrode properties in a multi-component system.

However, not all percolated TPBs are electrochemically active. Knowing the electrochemically active zone (EAZ) is useful for the design and optimization of an electrode's inter-layer structure. For example, using an inter-layer thickness that is smaller than the EAZ thickness will cause higher activation polarization. Using an inter-layer thickness that is much larger than the EAZ thickness will cause high ohmic and concentration polarizations.

The electrochemical reaction is driven by the balance of local equilibrium potentials that are affected by the electronic and ionic conductivities of the composite electrodes, the gas transport in the electrodes as well as operational conditions, such as output current density and operating temperature. A quantitative determination of electrochemical activity requires careful consideration of both the electric potential profile and the electrochemical potential distribution within the composite electrode. This cannot be achieved by the percolation theory based micro-model alone and requires a combined approach of micro-scale and macro-scale modeling. The cell-level scale macro-model is required to simulate simultaneously the gas transport, the ionic and electronic conductions, and the electrochemical reactions in an SOFC with porous composite electrodes, while required effective material properties may be provided by the electrode micro-model.

The main objective of this work is to study the detailed electrochemical and physical processes in an SOFC, and comprehensively analyze the factors that affect the performance of cathode inter-layer. For that purpose, an equivalent circuit model is proposed to represent the electrochemically active sites and the electron and ion conducting paths in an SOFC. With this model, the local electronic and ionic electric potential profiles in the electrode- and electrolyte-phases can be described based on local gas compositions and electrochemical kinetic analysis. Correspondingly, a cell-level scale macro-model, coupled with our particle-scale percolation micro-model [4], is developed to analyze the effects of thickness, material properties (such as exchange current density based on per TPB, electronic and ionic conductivities), operational conditions (such as temperature and output current density) and microstructure (such as the mean particle radius, electrode- and electrolyte-particle radial ratio, composition and porosity) on the performance of a cathode inter-layer, providing the theoretical basis for optimal design. The micro-scale and macro-scale coupled model is calibrated to the experimental data; however, the purpose of the combined modeling is not only to match the experimental data, but also to explore the parameter effects on cathode inter-layer performance and provide guidelines for a manufacturer of electrode development.

2. Theory

Due to the low ionic conductivity of the electrolyte-material, electrochemical reactions may occur only in a small region around the interface between the dense electrolyte layer and the electrode layer. This is believed to occur exclusively within the composite electrode inter-layer. However, which part of the electrode inter-layer could be a percolated TPB zone and what percentage of this zone can be electrochemically active are determined by many factors. The main factors influencing the EAZ are discussed below. As the activation overpotential is dominated by the electrochemical reactions at the cathode side, we focus our discussion on the EAZ of the cathode inter-layer.

2.1. Effect of electrode composition on EAZ

To facilitate a discussion of the effects of electrode composition on the EAZ, Fig. 2 shows three different representative electrode-particle loading scenarios for the cathode inter-layer.

(a) *Low electrode-particle loading*: Low electrode-particle loading occurs when the composite electrode inter-layer consists of a small portion of electrode-particles mixed with a large portion of electrolyte-particles. As illustrated in Fig. 2a, most of the electrolyte-particles belong to percolated clusters, while the electrode-particles can only form some short connecting networks near a cathode current collector. In this case, the percolated TPBs (noted with a bracket on the left) are found only close to the cathode current collector surface. These percolated TPBs, however, are only potentially electrochemically active. What percentage of these can be cathode EAZ (noted with a bracket on the right) depends on the ability of ions to be transported from dense electrolytes to the percolated TPBs. This, in turn, depends on the cathode inter-layer thickness and ionic conductivity. In a very thin electrode inter-layer, where ions can propagate throughout structure with relatively little potential losses, most of the percolated TPBs in Fig. 2a are electrochemically active. This behavior is observed experimentally when the polarization resistance does not depend strongly on the volume fraction of electrode composition [22,23]. In a relatively thick electrode inter-layer, however, ions cannot propagate at a significant distance from the dense electrolyte surface because of the low ionic conductivity of the electrolyte-particles (e.g., YSZ). In this case, the percolated TPBs near the current collector are essentially inactive. Again, this behavior is observed experimentally. In relatively thick composite electrodes, polarization resistance increases sharply before the electrode-particles are percolated [22,24].

(b) *Equivalent electrode-particle loading*: Equivalent electrode-particle loading occurs when there are similar electrode- and electrolyte-particles loadings. As shown in Fig. 2b, most of the

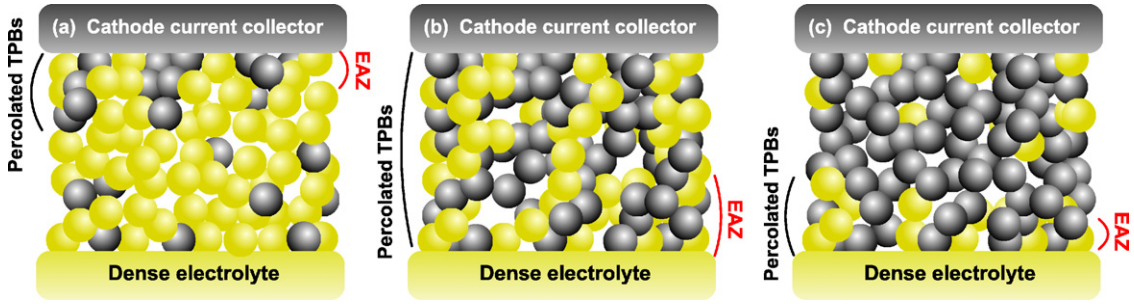

Fig. 2. Illustration of the cathode inter-layers with different loadings of electrode- (dark) and electrolyte- (light) particles: (a) low electrode-particle loading; (b) equivalent electrode-particle loading; (c) high electrode-particle loading. Brackets on the left indicate the regions of percolated TPBs. Brackets on the right indicate the electrochemically active zone (EAZ).

electrode- and electrolyte-particles are found to be percolated. In this case, the percolated TPBs are distributed throughout the structure. However, the cathode EAZ (noted with a bracket on the right) is concentrated near the dense electrolyte surface because of the relatively low ionic conductivity of the electrolyte-particles. As a result, there is an upper limited thickness, l_0, such that the EAZ can spread from the dense electrolyte surface to the electrode inter-layer. The remaining portion of the thick cathode inter-layer is electrochemically inactive. Using an inter-layer thickness that is smaller than l_0 may cause higher activation overpotential for the electrode. However, using an inter-layer thickness that is larger than l_0 may not further reduce the activation polarization, instead, it may cause higher ohmic and concentration polarization for the composite electrode. Therefore, l_0 is a useful parameter for the electrode design.

(c) *High electrode-particle loading*: This occurs when a small fraction of electrolyte-particles are mixed with a large portion of electrode-particles. As shown in Fig. 2c, most electrode-particles are percolated with increased electrode-particle loading, while the electrolyte-particles can only form short connecting paths near the dense electrolyte surface. In this case, the cathode percolated TPBs are concentrated near the dense electrolyte. High electrode-particle loading may come at the expense of too few electrolyte-particles and consequently too small percolated TPBs and EAZ. High activation polarization is often expected.

As discussed above, the electrode-particle loading determines the distribution of the percolated TPBs within the electrode inter-layer. The percolated TPBs are potentially electrochemically active. However, whether these percolated TPBs are truly electrochemically active is determined by other factors such as the thickness and effective ionic conductivity of the cathode inter-layer. In the following discussion, we focus our attention on the electrode inter-layer with equivalent electrode-particle loading.

2.2. Equivalent circuit model for the electric process

For an SOFC with composite electrodes illustrated in Fig. 2b, the electric process, including the electron and ion transfer paths and electrochemical reactions, can be represented by an equivalent circuit model shown in Fig. 3. As illustrated in Fig. 3, the electronic current of an operating cell, i_{op}, flows from an anode interconnect to an anode support to an anode inter-layer. The electronic current (i_e^a) is then converted into an ionic current (i_i) by electrochemical reaction (by oxidizing hydrogen fuel) at different EAZ locations in the anode inter-layer. That is, there are parallel paths for the electronic and ionic current conductions in the anode EAZ. All of the electronic current is converted to ionic current before entering the dense electrolyte. Purely ionic current is transported through the dense electrolyte to the cathode inter-layer where the ionic current is converted back into electronic current by an electrochemical reaction (by reducing oxygen) inside the EAZ of the cathode inter-layer. Purely electronic current is transported from the cathode inter-layer to the cathode current collector and then to the cathode interconnect. In Fig. 3, the local electrochemical reaction interfaces within the EAZ are represented by the parallel circuit within the dashed pane. The electromotive forces for the electrochemical reactions, E_a^{eq} and E_c^{eq}, are the differences of the local equilibrium electric potentials in the electrode- and electrolyte-phases.

As can be seen from the above discussion, the equivalent circuit model depicts an accurate picture of the electrical processes in an SOFC.

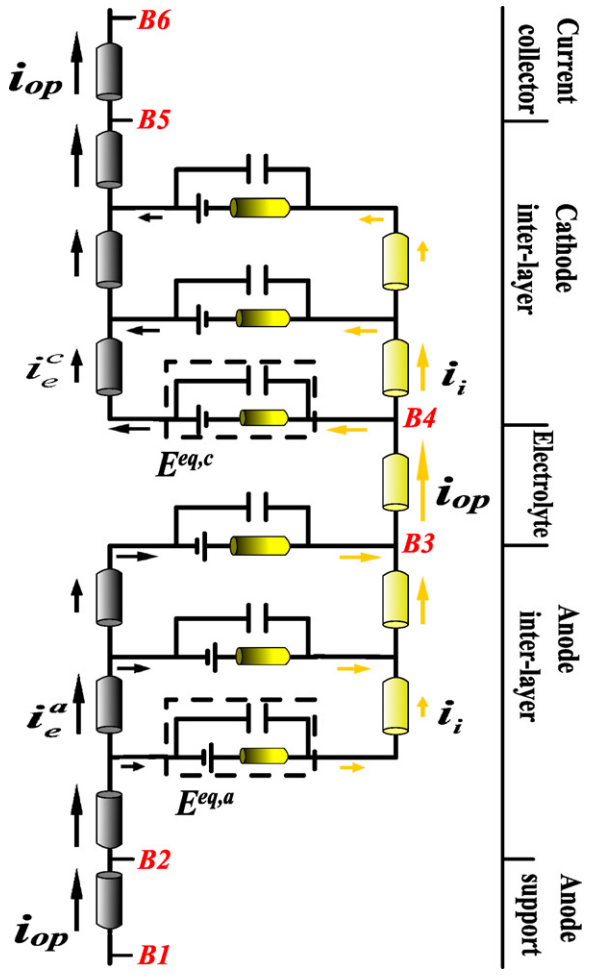

Fig. 3. Equivalent circuit model for the electrical process of an SOFC. Dark and light bricks indicate the electrode- and electrolyte-materials, respectively. B1, B2, B3, B4, B5 and B6 represent the interfaces between the anode interconnect, anode support, anode inter-layer, dense electrolyte, cathode inter-layer, cathode current collector and cathode interconnect, respectively. i_{op}, i_e and i_i are the output current density, local electronic and ionic current densities, respectively. The parallel circuit within the dashed pane represents the local electrochemical reaction interface, in which E_a^{eq} and E_c^{eq} are local equilibrium electric potential differences.

2.3. Mathematical description for the electrochemical process

The electrochemical reaction in the anode EAZ can be expressed as $H_2 + O^{2-} \rightleftharpoons H_2O + 2e^-$. At equilibrium (no net reaction), the electrochemical potentials of the reacting species should be balanced for the reaction, and we have [25],

$$\mu_{H_2} + \mu_{O^{2-}} - 2F\Phi_i^{eq} = \mu_{H_2O} - 2F\Phi_e^{a,eq}, \quad (1)$$

where μ_α is the chemical potential of species α, F is the Faraday constant. Φ_i^{eq} and $\Phi_e^{a,eq}$ are the local equilibrium electrical potentials of the electrolyte-phase and electrode-phase, respectively. The anode equilibrium electric potential difference between the two phases is as follows:

$$E_a^{eq} = \Phi_i^{eq} - \Phi_e^{a,eq} = \frac{1}{2F}(\mu_{H_2} + \mu_{O^{2-}} - \mu_{H_2O}) \quad (2)$$

Similarly, oxygen reduction inside cathode EAZ can be written as $1/2O_2 + 2e^- \rightleftharpoons O^{2-}$ and the equilibrium electrochemical potentials are related as:

$$0.5\mu_{O_2} - 2F\Phi_e^{c,eq} = \mu_{O^{2-}} - 2F\Phi_i^{eq} \quad (3)$$

The cathode equilibrium electric potential difference between the electrode-phase and the electrolyte-phase can then be expressed as follows:

$$E_c^{eq} = \Phi_e^{c,eq} - \Phi_i^{eq} = \frac{1}{4F}(\mu_{O_2} - 2\mu_{O^{2-}}). \quad (4)$$

At working conditions when there is electric current flowing through the cell, the local electric potentials, Φ_i, Φ_e^a and Φ_e^c, are different from their equilibrium values. The local activation overpotential, η_{act}, can be expressed, respectively, for the anodic and cathodic electrochemical reactions as follows:

$$\eta_{act}^a = E_a^{eq} - (\Phi_i - \Phi_e^a); \quad \eta_{act}^c = E_c^{eq} - (\Phi_e^c - \Phi_i). \quad (5)$$

The charge transfer rate per unit TPB length between the electronic and ionic current, j_{TPB} ($A\,m^{-1}$), can be evaluated with the empirical Butler–Volmer equation as follows [26]:

$$j_{TPB} = j_0 \left[\exp\left(\frac{2\alpha_f F}{RT}\eta_{act}\right) - \exp\left(\frac{-2\beta_r F}{RT}\eta_{act}\right)\right] \quad (6)$$

where R is the universal gas constant, T is the absolute temperature and α_f and β_r are the forward and reverse reaction symmetric factors, respectively. In this equation, j_0 is the local exchange transfer current per unit TPB length ($A\,m^{-1}$) and is often estimated as follows [7,27]:

$$j_0^c = j_{0,ref}^c \exp\left(-\frac{E_{O_2}}{R}\left(\frac{1}{T} - \frac{1}{T_{ref}}\right)\right)\left(\frac{p_{O_2}}{p_{O_2}^0}\right)^{0.25}$$
$$j_0^a = j_{0,ref}^a \exp\left(-\frac{E_{H_2}}{R}\left(\frac{1}{T} - \frac{1}{T_{ref}}\right)\right)\left(\frac{p_{H_2}p_{H_2O}}{p_{H_2}^0 p_{H_2O}^0}\right) \quad (7)$$

where E_{H_2} and E_{O_2} are the activation energies for the anode and cathode electrochemical reactions, respectively. Oftentimes $j_{0,ref}^a$ and $j_{0,ref}^c$ are deduced from experiments or assigned empirically at the reference temperature T_{ref}.

The charge transfer rate per unit volume ($A\,m^{-3}$) can then be expressed as $i_{e,i}^V = j_{TPB}\lambda_{TPB.eff}^V$, where $\lambda_{TPB.eff}^V$ is the percolated TPB length per unit volume (m^{-2}). The charge transfer rate per unit of dense electrolyte surface ($A\,m^{-2}$) is calculated as $i_{e,i}^S = j_{TPB}\lambda_{TPB.eff}^S$, where $\lambda_{TPB.eff}^S$ is the percolated TPB length per unit of electrolyte surface (m^{-1}).

To make solving the current conduction equations, which will be described later, more convenient, the local electric potentials are shifted by a reference amount as follows:

$$\hat{\Phi}_e^a = \Phi_e^a + \frac{1}{2F}(\mu_{H_2}^0 - \mu_{H_2O}^0), \quad \hat{\Phi}_e^c = \Phi_e^c - \frac{1}{4F}\mu_{O_2}^0,$$
$$\hat{\Phi}_i = \Phi_i - \frac{1}{2F}\mu_{O^{2-}}, \quad (8)$$

where μ_α^0 denotes the chemical potential of species α at the inlet of an anode or a cathode channel. The constant potential shift does not alter the electronic or ionic electric potential profiles within electrode- or electrolyte-phases of fuel cells, and different shifts may be adopted by different researchers [3,7,28]. Using Eq. (8) and the pressure dependence of the chemical potential of an ideal gas, Eq. (5) may be rewritten as follows:

$$\eta_{act}^a = \hat{\Phi}_e^a - \hat{\Phi}_i - \frac{RT}{2F}\ln\frac{p_{H_2}^0 p_{H_2O}}{p_{H_2}p_{H_2O}^0}; \quad \eta_{act}^c = \hat{\Phi}_i - \hat{\Phi}_e^c - \frac{RT}{4F}\ln\frac{p_{O_2}^0}{p_{O_2}}, \quad (9)$$

where p_α and p_α^0 are the partial pressure (atm) of species α at the local reacting site and the channel inlet, respectively. Eq. (9) shows that a local activation overpotential may be considered to be the corresponding difference between the local electronic potential, $\hat{\Phi}_e$, and the ionic potential, $\hat{\Phi}_i$, subtracted by the local concentration overpotential.

The cell output voltage, V_{op}, can be written as the difference between the electronic potentials at boundaries B1 and B6:

$$V_{op} = \Phi_e^c|_{B6} - \Phi_e^a|_{B1}. \quad (10)$$

Eq. (10) may be transformed in terms of Eq. (8) as,

$$\hat{\Phi}_e^c|_{B6} - \hat{\Phi}_e^a|_{B1} = V_{op} - E_O \quad (11)$$

where E_0 is the Nernst potential of the fuel and oxidant used and may be calculated as [28]:

$$E_0 = \frac{1}{2F}(\mu_{H_2}^0 + \frac{1}{2}\mu_{O_2}^0 - \mu_{H_2O}^0) = -\frac{\Delta G^0}{2F} + \frac{RT}{2F}\ln\frac{p_{H_2}^0 (p_{O_2}^0)^{0.5}}{p_{H_2O}^0}, \quad (12)$$

where ΔG^0 is the free energy change of the reaction $H_2 + 1/2O_2 \rightleftharpoons H_2O$ at the standard state.

2.4. Governing equations for electrical processes

The electrical processes are governed by electron conservation, ion conservation and Ohm's law. The volumetric charge transfer rate, $i_{e,i}^V$, at a local electrochemical reaction site can be viewed as a current source or leak. Consequently, the electric potentials obey the following charge conservation equations:

$$\nabla \cdot i_e^c = \nabla \cdot \left(-\sigma_{ed}^{eff}\nabla\hat{\Phi}_e^c\right) = \begin{cases} 0 & \text{in cathode current collector} \\ i_{e,i}^{V,c} & \text{in cathode inter-layer} \end{cases} \quad (13)$$

$$\nabla \cdot i_i = \nabla \cdot \left(-\sigma_{el}^{eff}\nabla\hat{\Phi}_i\right) = \begin{cases} -i_{e,i}^{V,c} & \text{in cathode inter-layer} \\ 0 & \text{in dense electrolyte} \\ i_{e,i}^{V,a} & \text{in anode support and inter-layer} \end{cases} \quad (14)$$

$$\nabla \cdot i_e^a = \nabla \cdot \left(-\sigma_{ed}^{eff}\nabla\hat{\Phi}_e^a\right) = -i_{e,i}^{V,a} \quad \text{in anode support and inter-layer} \quad (15)$$

where σ_{ed}^{eff} and σ_{el}^{eff} are the effective electronic and ionic conductivities, respectively. Here σ_{ed}^{eff} and σ_{el}^{eff} are determined by the material composition and are different for each of the five different layers of the cell. Because the anode support is usually made of a mixture of anode-material (Ni) and electrolyte-material (YSZ) for thermal compatibility, Eqs. (14) and (15) have, in principle, allowed a charge transfer reaction in the anode support in case the anode EAZ spreads beyond the anode inter-layer.

2.5. Governing equations for gas transport

The gas transport processes are governed by the mass balance equation:

$$\nabla \cdot N_\alpha = R_\alpha, \quad (16)$$

where N_α and R_α are the molar flux and reaction rate of species α, respectively. In this equation, R_α is calculated as $-i_{e,i}^{V,a}/2F$, $i_{e,i}^{V,a}/2F$, $-i_{e,i}^{V,c}/4F$ and zero for H_2, H_2O, O_2 and N_2, respectively. It is generally agreed that the dusty gas model is an accurate method for describing the gas transport in a porous media with small pore sizes [29]. For binary gas with species α and β, the dusty gas model may be expressed as [30–32],

$$\frac{N_\alpha}{D_{\alpha K}^{eff}} + \frac{x_\alpha N_\beta - x_\beta N_\alpha}{D_{\alpha\beta}^{eff}} = -\frac{1}{RT}(p\nabla x_\alpha + x_\alpha\nabla p + \frac{x_\alpha B_0 p}{\mu D_{\alpha K}^{eff}}\nabla p), \quad (17)$$

where x_α is the molar fraction of species α, B_0 the permittivity, μ the viscosity, p the total gas pressure, $D^{\text{eff}}_{\alpha K}$ the effective Knudsen diffusion coefficients of species α and $D^{\text{eff}}_{\alpha\beta}$ the effective binary diffusion coefficients.

The effective binary diffusivity can be estimated as [33],

$$D^{\text{eff}}_{\alpha\beta} = \frac{\phi_g}{\tau}\frac{3.24\times10^{-8}T^{1.75}}{p\left(\nu_\alpha^{1/3}+\nu_\beta^{1/3}\right)^2}\left(\frac{1}{M_\alpha}+\frac{1}{M_\beta}\right)^{0.5}, \tag{18}$$

where ϕ_g is the porosity, τ is the tortuosity, M_α *is* the molar mass, ν_α is the diffusion volume for species α ($\nu_\alpha = 6.12\times10^{-6}$, 13.1×10^{-6}, 16.3×10^{-6} and 18.5×10^{-6} $m^3\,mol^{-1}$ for H_2, H_2O, O_2 and N_2, respectively [33]).

The effective Knudsen diffusivity is calculated as [34],

$$D^{\text{eff}}_{\alpha K} = \frac{\phi_g}{\tau}\frac{2r_g}{3}\sqrt{\frac{8RT}{\pi M_\alpha}}, \tag{19}$$

where r_g is the mean hydraulic pore radius. The Knudsen diffusion is important when pore size is small in comparison with the mean free path of gas molecules. Gas molecules collide more frequently with the pore walls than with the other molecules.

2.6. Effective properties of porous composite electrode

Numerical modeling with the above governing equations requires a set of electrode property parameters to predict fuel cell performance. For a meaningful examination of the influences of the electrode microstructure and cell design on the fuel cell operations, the capability to provide effective electrode properties based on electrode microstructural characteristics is required. This is achieved by a coordination number based percolation micro-model that provides a convenient path for relating the effective electrode properties to the microstructure parameters [4,19,21,35].

Considering a binary system with a random packing of spheres corresponding to the electrode-particles (denoted as ed) and electrolyte-particles (denoted as el), the TPB length per unit volume can be estimated as,

$$\lambda^{V}_{TPB} = 2\pi\min(r_{ed}, r_{el})\ \sin\theta\left(n^{V}_{ed}Z_{ed,el}\right), \tag{20}$$

where θ is the angle of particle contact, assumed to be around 15° according to Costamagna et al. [22]. Here r_k (k = ed or el) is the radius of k-particle. Additionally, $n^V_k = 3(1-\phi_g)\psi_k/4\pi r_k^3$ is the number of k-particles per unit volume in a composite electrode [3,4]. Finally, ψ_k is the volume fraction of k-particles in a solid structure.

For the λ^V_{TPB} to be potentially electrochemically active, the participating particles must be percolated through the entire structure. The percolated TPB lengths per unit volume can be estimated as,

$$\lambda^{V}_{TPB,eff} = \lambda^{V}_{TPB}P_{ed}P_{el} \tag{21}$$

where the probability of k-particles belonging to percolated clusters can be estimated as [22],

$$P_k = \left(1-\left(\frac{3.764-Z_{k,k}}{2}\right)^{2.5}\right)^{0.4}. \tag{22}$$

The average number of ℓ-particles in contact with a k-particle can be estimated as [4],

$$Z_{k,\ell} = 0.5\left(1+r_k^2/r_\ell^2\right)\bar{Z}\frac{\psi_\ell/r_\ell}{\sum_{k=1}^{M}\psi_k/r_k}, \tag{23}$$

where $\bar{Z}$ is the overall average coordination number of all solid particles and M is the number of particle types. Here $\bar{Z}$ is set to six for a random packing of spheres [15,22,36] and M is two for binary systems. Eq. (23) satisfies the contact number conservation requirement for any ratio of r_k/r_l and is an important improvement over the previous theories [4].

Similarly, for the electrochemical reactions taking place at the electrolyte–electrode interface, the percolated TPB length per unit dense electrolyte surface area is calculated as,

$$\lambda^{S}_{TPB,eff} = 2\pi r_{ed}\ \sin\theta n^{S}_{ed}P_{ed}, \tag{24}$$

where the number of k-particles per unit dense electrolyte surface is [3,4],

$$n^S_k = \frac{(1-\phi_g)\psi_k}{2\pi r_k^2/3} \tag{25}$$

Moreover, the effective electric conductivity of the k-phase is determined as [37],

$$\sigma^{\text{eff}}_k = \sigma^0_k\left(\frac{\psi_k-\psi^t_k}{1+\phi_g/(1-\phi_g)-\psi^t_k}\right)^2, \tag{26}$$

where σ^0_k is the electric conductivity of k-material in a dense solid. In this equation, ψ^t_k is the threshold volume fraction of k-particles, which is determined by [4,22],

$$\bar{Z}\frac{\psi^t_{ed}/r_{ed}}{\psi^t_{ed}/r_{ed}+(1-\psi^t_{ed})/r_{el}} = 1.764;$$
$$\bar{Z}\frac{\psi^t_{el}/r_{el}}{(1-\psi^t_{el})/r_{ed}+\psi^t_{el}/r_{el}} = 1.764. \tag{27}$$

σ^0_k for Ni, LSM and YSZ may be estimated as [3,10],

$$\sigma^0_{Ni} = 3.27\times10^6 - 1065.3T$$
$$\sigma^0_{LSM} = \frac{4.2\times10^7}{T}\ \exp\left(\frac{-1150}{T}\right) \tag{28}$$
$$\sigma^0_{YSZ} = 6.25\times10^4\ \exp\left(\frac{-10300}{T}\right)$$

The parameters of σ^0_{YSZ} are deduced from the experimental values of 4.2 S m^{-1} at 800 °C and 1.6 S m^{-1} at 700 °C [1,38].

The hydraulic pore radius in the Knudson diffusivity expression (Eq. (19)) is calculated as [4],

$$r_g = \frac{2}{3}\frac{1}{1-\phi_g}\frac{1}{\psi_{ed}/r_{ed}+\psi_{el}/r_{el}}. \tag{29}$$

To test the validity of the percolation micro-model, the model predictions were compared with the recent FIB-SEM data of Wilson et al. [39] and Iwai et al. [40]. Fig. 4 shows the comparison of the measured λ^V_{TPB} and $\lambda^V_{TPB,eff}$ for $\phi_g = 0.5$, average diameter of 0.56 ± 0.4 μm for LSM-particles and 0.32 ± 0.2 μm for YSZ-particles [39] and the calculated values by the percolation micro-model at the same parameter setting and $\theta = 19.5°$ as a function of the YSZ volumetric fraction in solid content, ψ_{el}. The average contact angle θ, reflecting the overlap between particles, is not measured experimentally, but should be approximately constant for different ψ_{el} due to the use of a similar experimental procedure. This constant θ is the only fitting parameter in the micro-model. As shown in Fig. 4, there was good agreement between the measured and calculated data for different ψ_{el}. Moreover, agreement between the experimental data reported by Iwai et al. [40] and the percolation micro-mode can also be obtained with a larger particle size, consistent with the SEM image of Ref. [40] (Fig. 2b). The above analysis demonstrates the capability of the percolation micro-model to relate microstructure parameters with effective electrode properties.

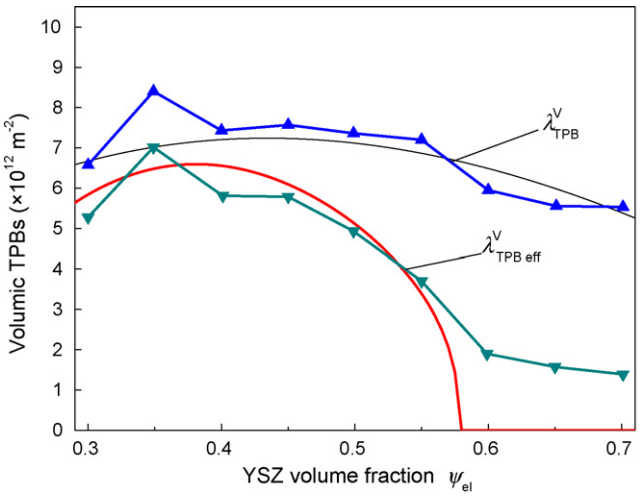

Fig. 4. Comparison of the FIB-SEM measured λ^{V}_{TPB} and $\lambda^{V}_{TPB,eff}$ and the calculated results by the percolation micro-model.

2.7. Numerical simulation

The finite element commercial software COMSOL MULTIPHSICS® Version 3.4 [41] was used in the present study to solve the coupled partial differential equations of electronic, ionic and gas transport macro-models described above in Sections 2.4 and 2.5. The effective properties for each material layer with different microstructures were calculated by the percolation micro-model described in Section 2.6. The boundary conditions required for all interfaces are shown in Table 1. Notice that boundary B1 for gas transport refers to the interface between the fuel channel and the anode support instead of the interface between the interconnect and the anode support that is appropriate for current conduction. Similarly, boundary B6 for gas transport refers to the interface between the cathode current collector and the air channel. Moreover, depending on the problem, total current density, i_{op}, may be used to replace V_{op} for the electronic current conduction boundary condition at boundary B6.

2.8. Basic modeling parameters

Model parameters were chosen to correspond to experimental data as much as possible. Table 2 lists the basic model parameters with the experimental sources specified. Theoretical parameters are often set to be consistent with experimental observations. For example, the values of r_{ed}/r_{el} in the cathode inter-layer and anode support were determined by the micro-model to reproduce the experimental conductivities of cathode inter-layer and anode support at 800 °C reported by Zhao and Virkar [1]. The values of σ^{eff}_{ed} and σ^{eff}_{ed} at 700 and 600 °C as well as most data for $\lambda^{V}_{TPB,eff}$, $\lambda^{S}_{TPB,eff}$ and other effective electrode properties were calculated from the microstructure data and shown in Table 2.

Based on the parameters in Table 2 and $p^0_{H_2} = 0.97$ atm, $p^0_{H_2O} = 0.03$ atm, and $p^0_{O_2} = 0.21$ atm, theoretical I–V curves may fit the experimental results very well, as shown in Fig. 5a. The fitting used $j^c_{0,ref}$ (T_{ref}=800 °C) and α^c_f as the fitting parameters and the experimentally deduced contact resistances [1] were also used. The term β^c_r is chosen to be $1 - \alpha^c_f$. The terms α^a_f and β^a_r are inconsequential so long as $j^a_{0,ref}$ is sufficiently large ($j^a_{0,ref}$ is estimated to be a factor of 50–100 larger than $j^c_{0,ref}$ [26]). The good agreement between the theoretical and experimental I–V curves demonstrates the suitability of our proposed theoretical description.

Table 1
Boundary conditions for solving the coupled partial differential equations of current conduction and gas transport. "Insulation" means there is no flux through the boundary.

	B1	B2	B3	B4	B5	B6
Ionic charge balance	Insulation	Continuity	$-n \cdot i_i = i^{S,a}_{e,i}$	$-n \cdot i_i = -i^{S,c}_{e,i}$	Continuity	Insulation
Electronic charge balance	E_0	Continuity	$-n \cdot i^a_e = -i^{S,a}_{e,i}$	$-n \cdot i^c_e = i^{S,c}_{e,i}$	Continuity	V_{op}
Mass balance	$p^0_{H_2} p^0_{H_2O}$	Continuity	$-n \cdot N_{H_2} = -i^{S,a}_{e,i}/2F$ $-n \cdot N_{H_2O} = i^{S,a}_{e,i}/2F$	$-n \cdot N_{O_2} = \frac{-i^{S,c}_{e,i}}{4F}$ $-n \cdot N_{N_2} = 0$	Continuity	$p^0_{O_2} p^0_{N_2}$

Table 2
The structural parameters and material properties of fuel cell layers.

	Current collector	Cathode inter-layer	Electrolyte	Anode inter-layer	Anode support
Thickness (μm)	50 [1]	20 [1]	8 [1]	20 [1]	1000 [1]
ϕ_g	45% [1]	26% [1]		23% [1]	48% [1]
ψ_{ed}	100% [1]	47.5% [1]		55% [1]	55% [1]
σ^{eff}_{ed} (S m^{-1})	4.05×10^3 800 °C	25.5 800 °C [1]		1413 800 °C	430 800 °C [1]
	4.00×10^3 700 °C	25.0 700 °C		1484 700 °C	451 700 °C
	3.90×10^3 600 °C	24.4 600 °C		1555 600 °C	473 600 °C
σ^{eff}_{el} (S m^{-1})		0.36 800 °C	4.2 800 °C [1]	0.31 800 °C	
		0.14 700 °C	1.6 700 °C [1]	0.12 700 °C	
		0.04 600 °C	0.47 600 °C	0.04 600 °C	
r_{ed}/r_{el}	1	1.85		2.71	2.71
r_{el} (μm)	0.6	0.2		0.2	0.3
r_g (μm)	0.72	0.23		0.27	0.53
$\lambda^{V}_{TPB,eff}$ (m^{-2})		2.71×10^{12}		1.53×10^{12}	
$\lambda^{S}_{TPB,eff}$ (m^{-1})		4.16×10^5		2.61×10^5	
E_{O_2} (J mol^{-1})		130×10^3 [7]			
α^c_f, β^c_r		0.65, 0.35			
$j^c_{0,ref}$ (A m^{-1})		1.25×10^{-4}			
E_{H_2} (J mol^{-1})				120×10^3 [7,27]	
$\alpha^a_f \beta^a_r$,				1, 0.5 [7,27]	
$j^a_{0,ref}$ (A m^{-1})				8.0×10^{-3}	
τ	3	3		3	3

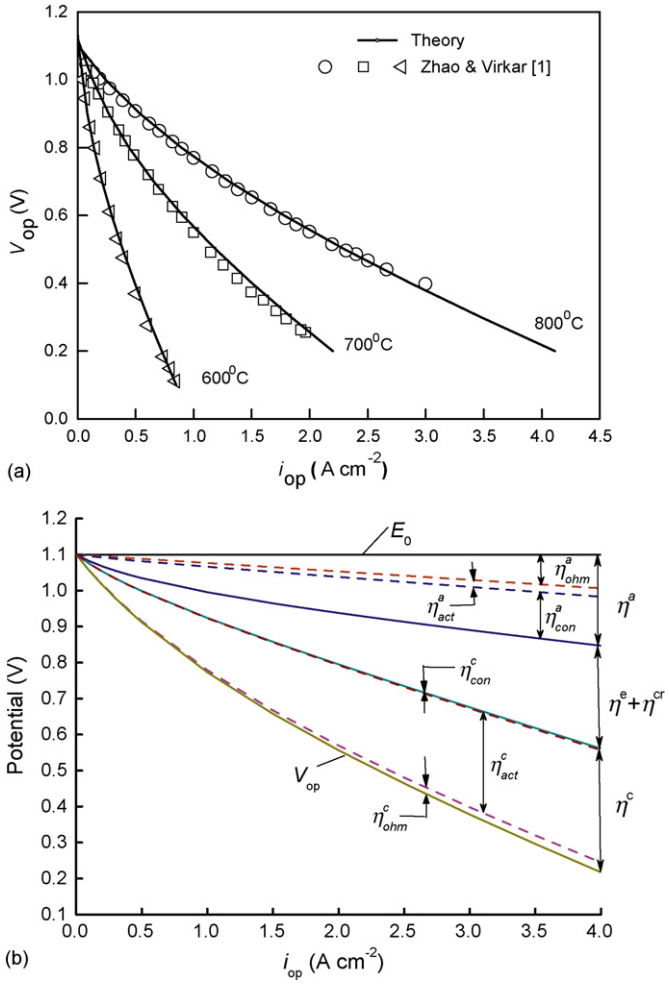

Fig. 5. (a) Comparison of theoretical and experimental *I–V* relationships at different temperatures. (b) The contribution of each polarization component to the total overpotential at 800 °C.

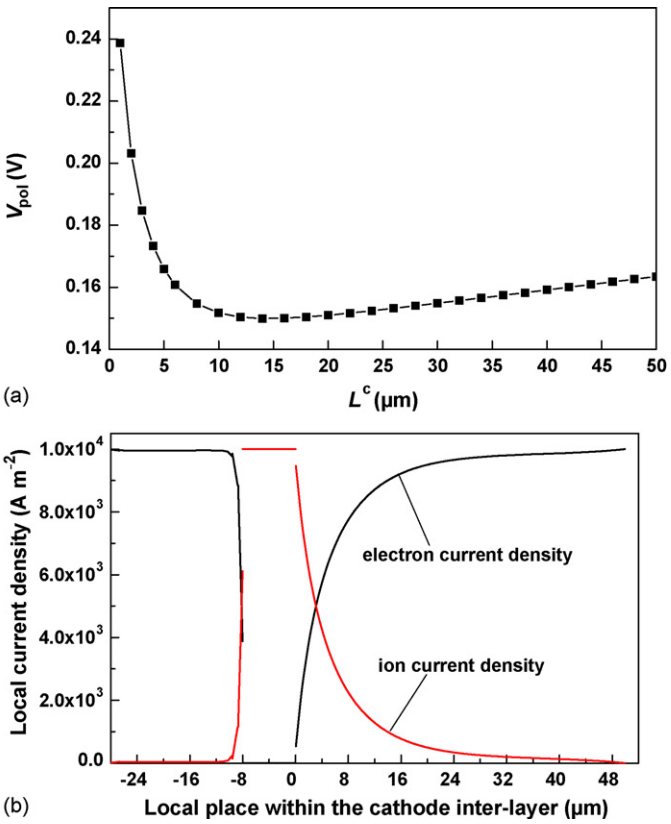

Fig. 6. (a) Variation of the overall polarization of the cathode inter-layer, V_{pol}, with the inter-layer thickness, L^c. (b) Distributions of electronic (black line) and ionic (red line) current densities within the assembly of anode inter-layer ($-28\,\mu m < l < -8\,\mu m$), electrolyte ($-8\,\mu m < l < 0\,\mu m$) and cathode inter-layer ($0\,\mu m < l < 50\,\mu m$). Discontinuities of the current density distribution at the electrode–electrolyte interfaces indicate the amount of current density conversion by electrochemical reactions at the interface TPBs. (For interpretation of the references to color in this figure legend, the reader is referred to the web version of the article.)

Fig. 5b shows the contribution of each polarization to the potential loss at 800 °C. Here η^a is the total polarization of the anode, i.e., the sum of the concentration polarization, η^a_{con}, ohmic polarization, η^a_{ohm}, and the activation polarization, η^a_{act}, of the anode. Both η^a_{con} and η^a_{ohm} are important due to the large thickness of anode support and its relatively low electric conductivity. The terms η^e and η^{cr} are the potential losses of dense electrolyte and interface contact resistance, respectively. The term η^c is the total polarization of the cathode, i.e., the sum of concentration polarization, η^c_{con}, ohmic polarization, η^c_{ohm}, and activation polarization, η^c_{act}, of the cathode. As shown in Fig. 5b, the relative importance of these polarization components is consistent with the conventional expectation, indicating that each of the electrode properties was described properly by the model.

Except for the cathode inter-layer thickness, the model parameters described above are used throughout the paper, unless specified otherwise. Unless stated otherwise, the operating temperature is 800 °C and the operating current density is 10^4 A m^{-2}.

3. Results and discussion

To examine the dependence of the performance of the cathode inter-layer on the material properties and microstructure parameters, we tried to vary only one basic model parameter at a time while keeping the others set at the standard values described in the last section.

3.1. Effect of the cathode inter-layer thickness

The dependence of the overall polarization of a cathode inter-layer, V_{pol}, on its thickness, L^c, is shown in Fig. 6a. The term V_{pol} includes the activation overpotential for the electrochemical reaction, the ohmic polarization for electric current conduction and the concentration polarization for gas transport in the porous cathode inter-layer. When L^c is close to zero, the ohmic and concentration polarizations are also close to zero. However, all ionic current must be transferred at the interface of the dense electrolyte and the cathode inter-layer, i.e., at the surface TPBs. This is possible only with a large activation overpotential. With an increase of L^c, an increasing amount of the ionic current may be converted in the TPBs inside the inter-layer, resulting in a reduced activation overpotential. Furthermore, as the ohmic and concentration polarizations were relatively small in comparison with the activation polarization, the overall potential loss of the inter-layer decreased. Because all oxygen ions produced inside the inter-layer must be transported to the dense electrolyte through the inter-layer with low ionic conductivity, most ionic current is produced near the dense electrolyte interface, as shown in Fig. 6b. In other words, only a limited thickness of the cathode inter-layer can support the electrochemical reaction for a charge transfer between the electronic and ionic currents, and the rest remains electrochemically inactive. Consequently, further increases of the inter-layer thickness beyond a certain value have virtually no effect on reducing the activation overpotential. On the other hand, the ohmic and concentration overpotential increases

with L^c, albeit only slightly. As a result, the overall polarization of the inter-layer decreased rapidly initially then increased gradually with L^c, as is evident in Fig. 6a. The minimal overall polarization was achieved with an inter-layer thickness of about 15 μm. Notice, however, any L^c in the range of 8–30 μm can be viewed as sufficiently optimal because the corresponding overall polarization is higher than the minimum by less than 5 mV.

3.2. Effect of material properties

Although YSZ and LSM are the most common electrolyte- and cathode-materials used in SOFC studies, there are also many other candidate materials. In fact, different experimental processing for the same material set can also result in very different effective properties. Examining the effects of material properties on the cell design is of practical importance. The effective material properties discussed here include the electronic and ionic conductivities and exchange current density based on per unit TPB length.

3.2.1. Effect of electronic conductivity

The overpotentials of a cathode inter-layer for a number of σ_{ed}^{eff} were calculated and the representative results are shown in Fig. 7. For a cathode inter-layer with low electronic conductivity ($\sigma_{ed}^{eff} = 5\,S\,m^{-1}$), V_{pol} was sensitive to the inter-layer thickness and a minimum of 160 mV was found at L^c = 10 μm. Allowing for a tolerance of 5 mV in minimizing V_{pol}, L^c should be in the range of (6, 16) μm. For intermediate to high σ_{ed}^{eff}, e.g., $\sigma_{ed}^{eff} > 15\,S\,m^{-1}$, V_{pol} was sensitive to thickness only for small L^c values. A minimum V_{pol} of 152 mV was found at L^c=13 μm for $\sigma_{ed}^{eff} = 15\,S\,m^{-1}$, and L^c in the range of (7, 24) μm was sufficiently optimal. For $\sigma_{ed}^{eff} = 250\,S\,m^{-1}$, a minimum V_{pol} of 146 mV was found at L^c = 20 μm and any thickness of L^c > 10 μm was sufficiently close to the optimal design. Overall, the use of L^c in the range of 10–16 μm was suitable for a cathode inter-layer with any practical σ_{ed}^{eff} to achieve near optimal performance. Because the upper limit of L^c at 16 μm was due to $\sigma_{ed}^{eff} = 5\,S\,m^{-1}$, which is improbably low for practical applications, it was safe to suggest a range of optimal L^c to be 10–20 μm.

3.2.2. Effect of ionic conductivity

Fig. 8 shows the results of the variation of V_{pol} with L^c for different σ_{el}^{eff}. The range of σ_{el}^{eff} examined was between 0.05 and 1.5 S m^{-1}. As shown in Table 2, σ_{el}^{eff} may be only 0.04 S m^{-1} when the working temperature is 600 °C. However, there are many other materials such as CeO_2 with much higher ionic conductivity and are more suitable than YSZ as the electrolyte-material when the working temperature is around 600 °C. Therefore, the chosen range of σ_{el}^{eff} is representative in practice. As shown in Fig. 8, the minimal V_{pol} was sensitive to σ_{el}^{eff}, but was less sensitive to L^c unless L^c was substantially smaller than the optimal value. The optimal L^c values were 5, 8, 11, 17, 23 and 27 μm for $\sigma_{el}^{eff} = 0.05$, 0.1, 0.2, 0.5, 1 and 1.5 S m^{-1}, respectively. The corresponding optimal V_{pol} were 249, 215, 179, 135, 106 and 92 mV, respectively. The observed results can be attributed to the fact that a larger σ_{el}^{eff} allowed more oxygen ions to be produced further away from the dense electrolyte interface, substantially reducing the activation overpotential with a smaller cost of ohmic overpotential. For a tolerance of 5 mV in V_{pol} minimization, the corresponding ranges of L^c were 2–18, 3–21, 5–25, 9–33, 13–41 and 15–47 μm for $\sigma_{el}^{eff} = 0.05$, 0.1, 0.2, 0.5, 1 and 1.5 S m^{-1}, respectively. Overall, an L^c in the range of 15–18 μm was almost optimal for all examined σ_{el}^{eff} ($0.05\,S\,m^{-1} < \sigma_{el}^{eff} < 1\,S\,m^{-1}$). The low limit was due to an improbably high σ_{el}^{eff} and the high limit is due to an improbably low σ_{el}^{eff}. For practical σ_{el}^{eff}, L^c in the range of 10–20 μm should be sufficiently optimal.

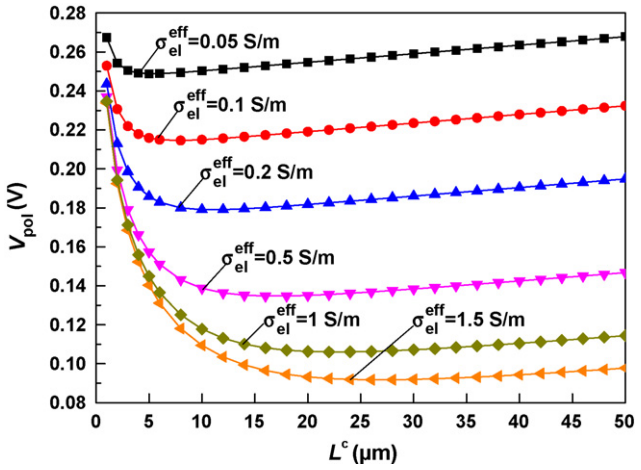

Fig. 8. Dependence of V_{pol} on L^c for cathode inter-layers with different effective ionic conductivities, σ_{el}^{eff}.

3.2.3. Effect of exchange current density

Fig. 9 shows the variation of V_{pol} with L^c for $3 \times 10^{-5}\,A\,m^{-1} < j_{0,ref}^c < 10^{-3}\,A\,m^{-1}$. A higher $j_{0,ref}^c$ means a lower activation over-

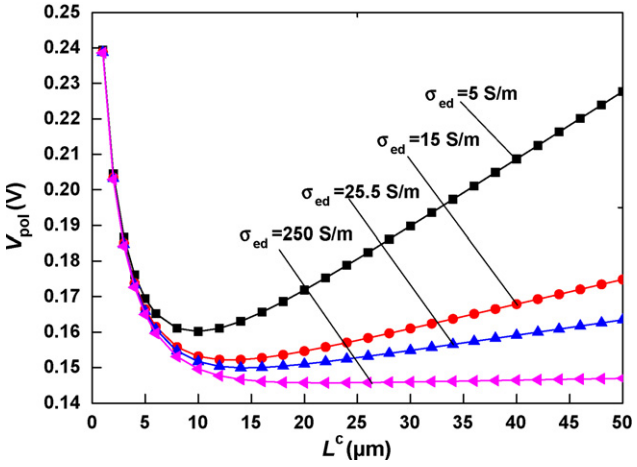

Fig. 7. Dependence of V_{pol} on L^c for cathode inter-layers with different effective electronic conductivities, σ_{ed}^{eff}.

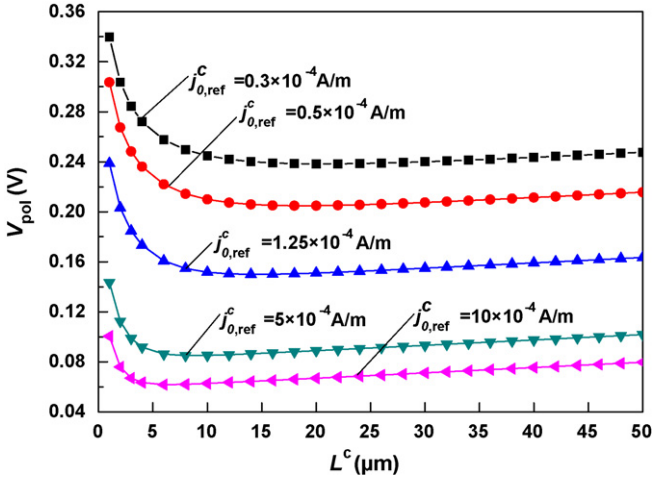

Fig. 9. Dependence of V_{pol} on L^c for cathode inter-layers with different exchange current density parameters, $j_{0,ref}^c$.

potential for the conversion of a given amount of electronic or ionic current. Naturally, V_{pol} decreases with the increase of $j^c_{0,ref}$. Moreover, a reduced activation overpotential with higher $j^c_{0,ref}$ also increases the relative importance of ohmic and concentration polarization. This causes an increased portion of the charge transfer reaction to take place at the dense electrolyte interface and the nearby inter-layer region. As a result, the minimum level of V_{pol} was found with a smaller L^c for higher $j^c_{0,ref}$, as shown in Fig. 9. The optimal thicknesses are 21, 19, 15, 9 and 6 μm for $j^c_{0,ref} = 0.3 \times 10^{-4}$, 0.5×10^{-4}, 1.25×10^{-4}, 5×10^{-4} and 10^{-3} A m^{-1}, respectively. Considering the tolerance of 5 mV for minimizing V_{pol}, 10 μm < L^c < 20 μm satisfies the requirement for any $j^c_{0,ref}$ in the range of 0.3×10^{-4} and 1.0×10^{-3} A m^{-1}.

3.3. Effect of operating conditions

We assumed in our modeling that the fuel cell is isothermal at 800 °C with a fixed output current density of 10^4 A m^{-2}. The output current density may vary due to different designs or load requirements. In fact, the current density generation in a working planar SOFC can vary substantially across the cell plate [42]. Similarly, SOFCs can be targeted for different working temperatures, and a working cell is not isothermal. The influences of these two common working parameters on cathode inter-layer performance are examined here.

3.3.1. Effect of output current density

Fig. 10 shows the influence of the output current density, i_{op}, on the variation of V_{pol} with L^c. Naturally, a higher i_{op} requires a larger V_{pol}. As the ohmic and concentration overpotential increased approximately linearly with the current density, V_{pol} increased linearly with L^c when L^c was larger than the EAZ thickness, and the slope was larger for a larger i_{op}. As a result, the minimum level of V_{pol} was found at a smaller L^c for a larger i_{op}, as can be seen in Fig. 10. The optimal thicknesses were 19, 17, 15 and 12 μm for $i_{op} = 0.3 \times 10^4$, 0.6×10^4, 10^4 and 1.5×10^4 A m^{-2}, respectively. Assuming a tolerance of 5 mV for minimizing V_{pol}, the corresponding ranges of L^c are 8–60, 8–41, 7–31 and 6–24 μm, respectively. The limited sensitivity of the desirable L^c range on the output current density was satisfactory as it meant an optimal design could be found for all practical working currents. Indeed, 8 μm < L^c < 24 μm satisfied the design requirement for all i_{op} examined.

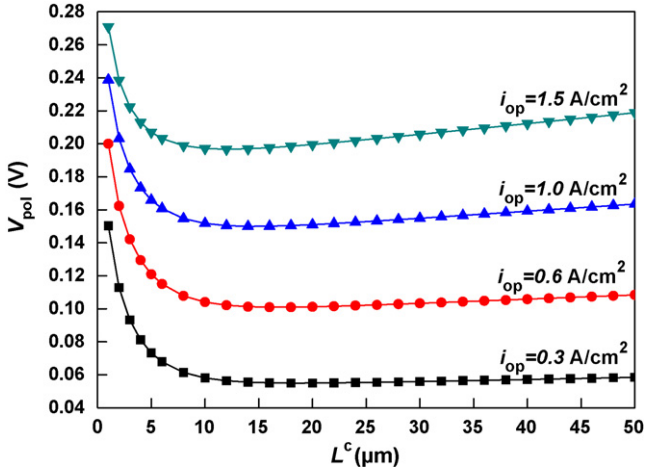

Fig. 10. Dependence of V_{pol} on L^c for different operating current densities, i_{op}.

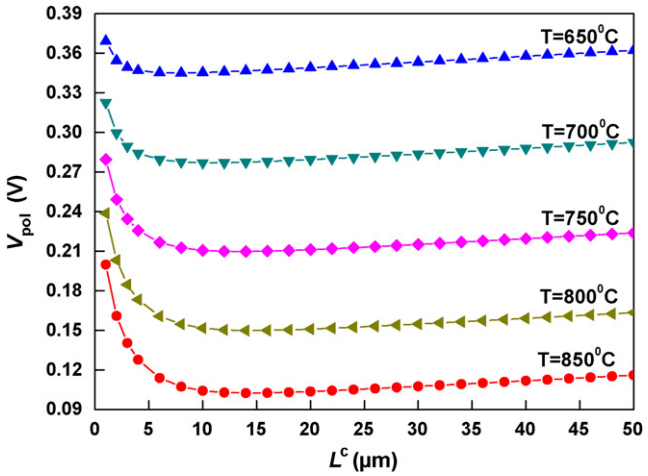

Fig. 11. Dependence of V_{pol} on L^c for different operating temperatures, T.

3.3.2. Effect of working temperature

Several material properties were strongly dependent on temperature. The ionic conductivity of the electrolyte-material increased with the temperature exponentially (Eqs. (28) and (26)). Here σ^{eff}_{el} varied from 0.076 to 0.55 S m^{-1} when T is changed from 650 to 850 °C. Additionally, j^c_0 increased with T, resulting in a smaller activation overpotential for the same charge transfer rate (Eqs. (7) and (6)). In addition, σ^{eff}_{ed} changed moderately, varying from 24.8 to 25.5 S m^{-1} when T varied from 650 °C to 850 °C. Overall, the change of σ^{eff}_{el} was the predominant temperature effect. Consequently, the temperature effect was qualitatively similar to the effect of ionic conductivity discussed in Section 3.2.2.

Fig. 11 shows the influence of T on the variation of V_{pol} with L^c. The optimal L^c was found at 8, 11, 13, 15 and 14 μm for T = 650, 700, 750, 800 and 850 °C, respectively. The corresponding ranges of L^c in μm are, respectively, 3–23, 4–27, 6–30, 8–31 and 8–30 when allowing for a tolerance of 5 mV to minimize V_{pol}. Overall, 8 μm < L^c < 23 μm was the range of optimal cathode inter-layer thickness for all temperatures examined.

3.4. Effect of microstructure on cell performance

As can be seen from the discussions in Section 2, the microstructural parameters for the cathode inter-layer can be summarized as the size of the electrolyte-particle r_{el}, the ratio of the electrolyte- and electrode-particles radii r_{ed}/r_{el}, the volume fraction of electrode-particle ψ_{ed} and the porosity ϕ_g.

3.4.1. Effect of r_{el}

The terms $\lambda^V_{TPB,eff}$, $\lambda^S_{TPB,eff}$ and r_g changed when r_{el} varied. Additionally, r_{ed} changed as r_{ed}/r_{el} was kept constant. As shown in Section 2.6, $\lambda^V_{TPB,eff}$ was proportional to the inverse square of r_{el}, and $\lambda^S_{TPB,eff}$ and r_g were proportional to the inverse of r_{el}. In addition, r_g only affected the gas transport in the inter-layer. Because the concentration polarization of the inter-layer was relatively small in all cases, variation of r_g had very limited influence on the inter-layer performance. The effects of changing $\lambda^V_{TPB,eff}$ and $\lambda^S_{TPB,eff}$ were significant as they influenced the activation overpotential directly.

The variations of V_{pol} with L^c for various r_{el} are shown in Fig. 12. Naturally, V_{pol} decreased with increases of $\lambda^V_{TPB,eff}$ and $\lambda^S_{TPB,eff}$ for smaller r_{el}. Reduced activation polarization increased the relative importance of the ohmic and concentration polarization, and the optimal L^c for minimizing V_{pol} was found at a smaller value for a smaller r_{el}, as shown in Fig. 12. The optimal thicknesses were 9, 15, 21 and 23 μm for r_{el} = 0.1, 0.2, 0.4 and 0.6 μm, respectively. Assum-

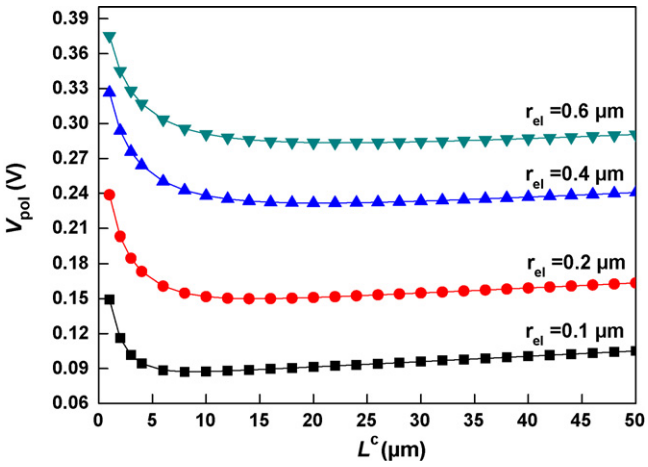

Fig. 12. Dependence of V_{pol} on L^c for different radii of electrolyte-particle, r_{el}.

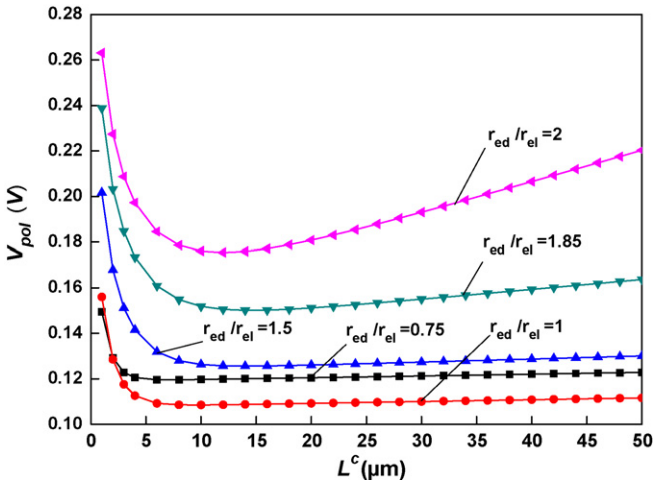

Fig. 13. Dependence of V_{pol} on L^c for different r_{ed}/r_{el}.

ing a tolerance of 5 mV for minimizing V_{pol}, 12 μm < L^c < 22 μm satisfied the optimal requirement for all r_{el} examined.

3.4.2. *Effect of relative particle sizes, r_{ed}/r_{el}*

As described in Section 2.6, σ_{el}^{eff}, σ_{ed}^{eff}, $\lambda_{TPB,eff}^{V}$, $\lambda_{TPB,eff}^{S}$ and r_g changed with a change of r_{ed}/r_{el}. Table 3 shows the variations of these property parameters on the values of r_{ed}/r_{el} in a range of 0.5–2. For r_{ed}/r_{el} = 0.5, there were many more electrode-particles than the electrolyte-particle in the cathode inter-layer for a fixed ψ_{ed} at 47.5%. The connectivity of the electrode-particle network was well above the percolation threshold, and σ_{ed}^{eff} was high. However, the connectivity of the electrolyte-particle network was only slightly above the percolation threshold, and σ_{el}^{eff} was low. Along with an increase of r_{ed}/r_{el}, σ_{el}^{eff} increased while σ_{ed}^{eff} decreased as observed experimentally [2]. The factors $\lambda_{TPB,eff}^{V}$ and $\lambda_{TPB,eff}^{S}$ also decreased with an increase of r_{ed}/r_{el} due to the reduced number of electrode-particles in a given volume of the inter-layer or the dense electrolyte surface, although this was compensated for in part by the improved connectivity of the network of the electrolyte-particles. The variation of r_g on r_{ed}/r_{el} was simple and was determined by Eq. (29).

The variations of V_{pol} with L^c for various r_{ed}/r_{el} are shown in Fig. 13. For r_{ed}/r_{el} < 1, the minimum level of V_{pol} decreased with an increase of r_{ed}/r_{el} as the benefits of the rapid increase of σ_{el}^{eff} outweighed the drawback of the decreased $\lambda_{TPB,eff}^{V}$ and $\lambda_{TPB,eff}^{S}$. For r_{ed}/r_{el} > 1, V_{pol} increased with an increase of r_{ed}/r_{el} caused by the rapid decreases of σ_{ed}^{eff}, $\lambda_{TPB,eff}^{V}$ and $\lambda_{TPB,eff}^{S}$, while the increase of σ_{el}^{eff} was only moderate. The lowest V_{pol} was found when r_{ed}/r_{el} = 1, reflecting the best-balanced parameter set of σ_{el}^{eff}, σ_{ed}^{eff}, $\lambda_{TPB,eff}^{V}$ and $\lambda_{TPB,eff}^{S}$. The minimum level of V_{pol} was found at different L^c for different r_{ed}/r_{el}. However, if a tolerance of 5 mV for minimizing V_{pol} was assumed, 8 μm < L^c < 20 μm satisfied the optimal requirement for all r_{ed}/r_{el} examined.

3.4.3. *Effect of inter-layer composition, ψ_{ed}*

According to Eqs. (22) and (23), the percolation threshold for the inter-layer electrode- and electrolyte-particles can be calculated as ψ_{ed}^{t} = 0.435 and $1 - \psi_{el}^{t}$ = 0.816 for r_{ed}/r_{el} = 1.85, respectively. Here ψ_{ed} < 0.435 corresponded to the cases illustrated in Fig. 2a, and the performance of cathode inter-layer is expected to be poor unless L^c is close to zero. Similarly, ψ_{ed} > 0.816 corresponded to the cases illustrated in Fig. 2c, and the performance of the cathode inter-layer was expected to decrease with an increase of L^c. However, the effect of L^c on the inter-layer's performance when ψ_{ed} > 0.816 was limited due to the high electronic conductivity and minimal gas transport resistance of the inter-layer. Therefore, we discussed cases where ψ_{ed} > 0.435. The values of ψ_{ed} discussed were 0.475, 0.55, 0.63, 0.7 and 1; ψ_{ed} = 1corresponded to a purely electronic conducting cathode inter-layer.

Table 3
Dependences of σ_{el}^{eff}, σ_{ed}^{eff}, $\lambda_{TPB,eff}^{V}$, $\lambda_{TPB,eff}^{S}$ and r_g on r_{ed}/r_{el} for r_{el} = 0.2 μm, ψ_{ed} = 47.5% and ϕ_g = 26%.

r_{ed}/r_{el}	σ_{ed}^{eff} (S m^{-1})	σ_{el}^{eff} (S m^{-1})	$\lambda_{TPB,eff}^{S}$ (m^{-1})	$\lambda_{TPB,eff}^{V}$ (m^{-2})	r_g (m)
0.5	883	0.026	2.73×10^{6}	1.26×10^{13}	0.12×10^{-6}
0.75	607	0.12	1.8×10^{6}	1.17×10^{13}	0.16×10^{-6}
1	393	0.20	1.28×10^{6}	9.90×10^{12}	0.18×10^{-6}
1.5	117	0.31	6.94×10^{5}	4.69×10^{12}	0.21×10^{-6}
1.85	25.3	0.36	4.16×10^{5}	2.71×10^{12}	0.23×10^{-6}
2	7.06	0.38	2.98×10^{5}	1.92×10^{12}	0.24×10^{-6}

Table 4
Variations of σ_{el}^{eff}, σ_{ed}^{eff}, $\lambda_{TPB,eff}^{V}$, $\lambda_{TPB,eff}^{S}$ and r_g with ψ_{ed} for r_{el} = 0.2 μm, r_{ed}/r_{el} = 1.85 and ϕ_g = 26%.

ψ_{ed}	σ_{ed}^{eff} (S m^{-1})	σ_{el}^{eff} (S m^{-1})	$\lambda_{TPB,eff}^{S}$ (m^{-1})	$\lambda_{TPB,eff}^{V}$ (m^{-2})	r_g (m)
0.475	25.3	0.359	4.16×10^{5}	2.71×10^{12}	0.23×10^{-6}
0.55	210	0.218	6.99×10^{5}	4.08×10^{12}	0.24×10^{-6}
0.63	606	0.107	9.25×10^{5}	4.56×10^{12}	0.25×10^{-6}
0.7	1120	0.0416	1.08×10^{6}	4.16×10^{12}	0.27×10^{-6}
1	7339	0	1.55×10^{6}	0	0.33×10^{-6}

Table 5
Variations of σ_{el}^{eff}, σ_{ed}^{eff}, $\lambda_{TPB,eff}^{V}$, $\lambda_{TPB,eff}^{S}$ and r_g with ϕ_g for r_{el} = 0.2 μm, r_{ed}/r_{el} = 1.85 and ψ_{ed} = 47.5%..

ϕ_g	σ_{ed}^{eff} (S m^{-1})	σ_{el}^{eff} (S m^{-1})	$\lambda_{TPB,eff}^{S}$ (m^{-1})	$\lambda_{TPB,eff}^{V}$ (m^{-2})	r_g (m)
0.10	46.57	0.56874	5.06×10^5	3.29×10^{12}	0.19×10^{-6}
0.20	32.047	0.43023	4.50×10^5	2.93×10^{12}	0.21×10^{-6}
0.26	25.349	0.35878	4.16×10^5	2.71×10^{12}	0.23×10^{-6}
0.36	16.743	0.2573	3.60×10^5	2.34×10^{12}	0.27×10^{-6}
0.46	10.602	0.17578	3.03×10^5	1.97×10^{12}	0.32×10^{-6}

As shown in Section 2.6, σ_{el}^{eff}, σ_{ed}^{eff}, $\lambda_{TPB,eff}^{V}$, $\lambda_{TPB,eff}^{S}$ and r_g changed with a change of ψ_{ed}. Table 4 shows the variations of these property parameters on the values of ψ_{ed}. The variations of V_{pol} with L^c for various ψ_{ed} are shown in Fig. 14. The lowest V_{pol} was found when ψ_{ed} = 0.55 at L^c = 13 μm due to the best-balanced parameter set of σ_{el}^{eff}, σ_{ed}^{eff}, $\lambda_{TPB,eff}^{V}$ and $\lambda_{TPB,eff}^{S}$. However, the parameter set for the cathode inter-layer of Zhao and Virkar (ψ_{ed} = 0.475) was very close to being optimal given that V_{pol} at L^c = 15 μm was only 2 mV above the global minimum. The minimum value of V_{pol} for ψ_{ed} = 1 was about twice the global minimum, agreeing with the widely reported experimental findings that a composite electrode exhibits lower activation overpotential than a single phase electrode made of pure electronic conducting material [35,43].

As shown in Fig. 14, the sensitivity of V_{pol} to L^c when L^c is small was quite different for different ψ_{ed}. However, in most cases, V_{pol} is insensitive to L^c when L^c was larger than the optimal value. Overall, 8 μm < L^c < 30 μm was the range of optimal inter-layer thickness for all ψ_{ed} examined, if we assumed a tolerance of 5 mV for minimizing V_{pol}.

3.4.4. Effect of porosity, ϕ_g

When there is a close packing of spherical particles, ϕ_g = 0.26 was expected. A smaller ϕ_g was possible by using an advanced processing procedure, and ϕ_g = 0.2 was the smallest ϕ_g reported for a working electrode inter-layer [6]. As shown in Table 5, all of the important property parameters, σ_{el}^{eff}, σ_{ed}^{eff}, $\lambda_{TPB,eff}^{V}$ and $\lambda_{TPB,eff}^{S}$, decreased with an increase of ϕ_g. Naturally, the performance of the cathode inter-layer was higher for smaller ϕ_g, as shown in Fig. 15. The cathode inter-layer performance could be improved with a further reduction of ϕ_g if the connectivity of the gas pores is maintained properly as assumed in our micro-model. However, maintaining gas pore connectivity might not be easy experimentally, and the guidelines provided here should be used with caution.

The minimum value of V_{pol} was found at L^c = 17, 16, 15, 12 and 9 μm for ϕ_g = 0.1, 0.2, 0.26, 0.36 and 0.46, respectively. Overall, 9 μm < L^c < 18 μm was the range of optimal inter-layer thickness for all ϕ_g examined when assuming a tolerance of 5 mV for minimizing V_{pol}. The upper limit of the optimal L^c was due to an unrealistically high ϕ_g and may be safely extended to 20 μm in practice.

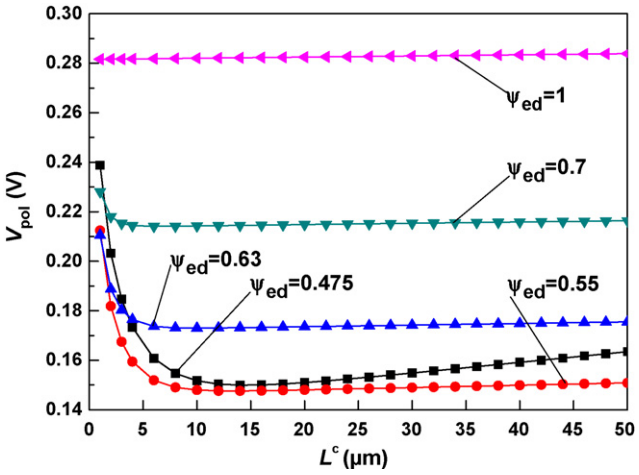

Fig. 14. Dependence of V_{pol} on L^c for different ψ_{ed}.

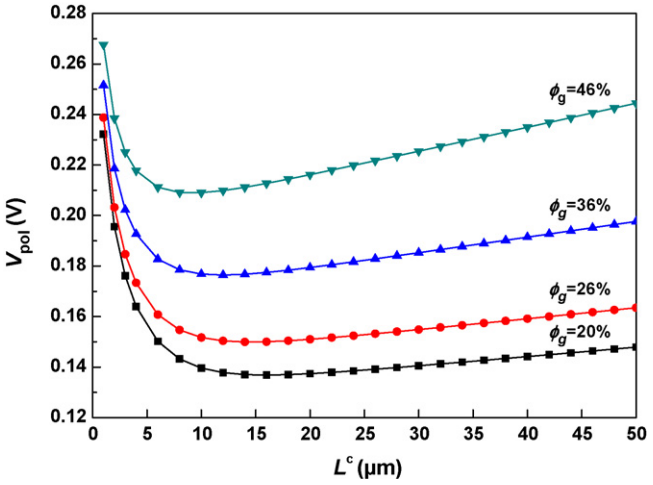

Fig. 15. Dependence of V_{pol} on L^c for different ϕ_g.

4. Summary

The processes of electrochemical reaction, electronic and ionic current conductions and gas transports in an SOFC were discussed and illustrated schematically. The schematic illustration provides a way for the broad SOFC community to easily understand the complicated multi-physics processes in SOFC.

We described in detail the mathematics required for the corresponding macro-model and a micro-model to deduce from the microstructure parameters what effective properties were required by the macro-model. The macro-model and micro-model were used to study the dependence of the performance of cathode inter-layer on its thickness, effective electronic and ionic conductivities, exchange current density, operating temperature, output current density, electrode- and electrolyte-particle radii, composition and porosity, with a focus on finding the optimal inter-layer thickness that minimizes the overall polarization of the cathode inter-layer. Assuming a tolerance of 5 mV for minimizing the polarization of the cathode inter-layer, an inter-layer thickness of 15 μm was found to be optimal for all parameter sets examined. Excluding unrealistic material parameters such as very high ionic conductivity or very low electronic conductivity of the cathode inter-layer, a cathode inter-layer thickness in the range of 10–20 μm was optimal for all practical situations. The conclusions drawn by our comprehensive study are simple and robust and should be very useful to researchers in the field.

Acknowledgements

We gratefully acknowledge the financial support of the Knowledge Innovation Program and the Key Program of the Chinese

Academy of Sciences (KJCX1.YW.07), the National High-tech R&D Program of China (2007AA05Z156) and the National Science Foundation of China (10574114).

References

[1] F. Zhao, A.V. Virkar, J. Power Sources 141 (1) (2005) 79–95.
[2] J.H. Yu, G.W. Park, S. Lee, S.K. Woo, J. Power Sources 163 (2) (2007) 926–932.
[3] D.H. Jeon, J.H. Nam, C.J. Kim, J. Electrochem. Soc. 153 (2) (2006) A406–A417.
[4] D.F. Chen, Z.J. Lin, H.Y. Zhu, R.J. Kee, J. Power Sources 191 (2009) 240–252.
[5] M.M. Hussain, X. Li, I. Dincer, Int. J. Hydrogen Energy 34 (7) (2009) 3134–3144.
[6] J.R. Wilson, W. Kobsiriphat, R. Mendoza, H.Y. Chen, J.M. Hiller, D.J. Miller, K. Thornton, P.W. Voorhees, S.B. Adler, S.A. Barnett, Nat. Mater. 5 (7) (2006) 541–544.
[7] H.Y. Zhu, R.J. Kee, J. Electrochem. Soc. 155 (7) (2008) B715–B729.
[8] J.R. Izzo, A.S. Joshi, K.N. Grew, W.K.S. Chiu, A. Tkachuk, S.H. Wang, W.B. Yun, J. Electrochem. Soc. 155 (5) (2008) B504–B508.
[9] A.V. Virkar, J. Chen, C.W. Tanner, J.W. Kim, Solid State Ionics 131 (1/2) (2000) 189–198.
[10] Y.X. Shi, N.S. Cai, C. Li, J. Power Sources 164 (2) (2007) 639–648.
[11] W. Zhou, Z.P. Shao, R. Ran, R. Cai, Electrochem. Commun. 10 (10) (2008) 1647–1651.
[12] M. Shah, J.D. Nicholas, S.A. Barnett, Electrochem. Commun. 11 (1) (2009) 2–5.
[13] Z.Y. Jiang, L. Zhang, K. Feng, C.R. Xia, J. Power Sources 185 (1) (2008) 40–48.
[14] S.P. Jiang, W. Wang, Y.D. Zhen, J. Power Sources 147 (1/2) (2005) 1–7.
[15] D. Bouvard, F.F. Lange, Acta Metall. Mater. 39 (12) (1991) 3083–3090.
[16] M. Suzuki, T. Oshima, Powder Technol. 35 (1983) 159–166.
[17] C.W. Tanner, K.Z. Fung, A.V. Virkar, J. Electrochem. Soc. 144 (1) (1997) 21–30.
[18] S. Sunde, J. Electrochem. Soc. 142 (4) (1995) L50–L52.
[19] A. Ali, X. Wen, K. Nandakumar, B.J. Luo, K.T. Chuang, J. Power Sources 185 (2) (2008) 961–966.
[20] S.H. Chan, X.J. Chen, K.A. Khor, J. Electrochem. Soc. 151 (1) (2004) A164–A172.
[21] V.M. Janardhanan, V. Heuveline, O. Deutschmann, J. Power Sources 178 (1) (2008) 368–372.
[22] P. Costamagna, P. Costa, V. Antonucci, Electrochim. Acta 43 (3–4) (1998) 375–394.
[23] T. Saito, Y. Akiyama, N. Ishida, T. Yasuo, S. Taniguchi, S. Murakami, N. Furukawa, Denki Kagaku 61 (2) (1993) 228–233.
[24] T. Kawada, N. Sakai, H. Yokokawa, M. Dokiya, M. Mori, T. Iwata, Solid State Ionics 40 (1) (1990) 402–406.
[25] R.J. Kee, H. Zhu, D.G. Goodwin, J. Combust. Soc. Jpn. 47 (2005) 192–204.
[26] R.P.O. Hayre, S.W. Cha, W. Colella, F.B. Frinz, Fuel Cell Fundamentals, John Wiley & Sons, 2006.
[27] P. Costamagna, K. Honegger, J. Electrochem. Soc. 145 (11) (1998) 3995–4007.
[28] S.X. Liu, C. Song, Z.J. Lin, J. Power Sources 183 (1) (2008) 214–225.
[29] K. Tseronis, I.K. Kookos, C. Theodoropoulos, Chem. Eng. Sci. 63 (23) (2008) 5626–5638.
[30] R. Krishna, J.A. Wesselingh, Chem. Eng. Sci. 52 (6) (1997) 861–911.
[31] R. Suwanwarangkul, E. Croiset, M.W. Fowler, P.L. Douglas, E. Entchev, M.A. Douglas, J. Power Sources 122 (1) (2003) 9–18.
[32] R. Suwanwarangkul, E. Croiset, E. Entchev, S. Charojrochkul, M.D. Pritzker, M.W. Fowler, P.L. Douglas, S. Chewathanakup, H. Mahaudom, J. Power Sources 161 (1) (2006) 308–322.
[33] B. Todd, J.B. Young, J. Power Sources 110 (1) (2002) 186–200.
[34] J.W. Veldsink, R.M.J. Vandamme, G.F. Versteeg, W.P.M. Vanswaaij, Chem. Eng. J. Biochem. Eng. 57 (2) (1995) 115–125.
[35] X.J. Chen, S.H. Chan, K.A. Khor, Electrochim. Acta 49 (11) (2004) 1851–1861.
[36] M. Suzuki, T. Oshima, Powder Technol. 44 (1985) 213–218.
[37] J.J. Wu, D.S. McLachlan, Phys. Rev. B 56 (3) (1997) 1236–1248.
[38] K. Sasaki, J.P. Wurth, R. Gschwend, M. Godickemeier, L.J. Gauckler, J. Electrochem. Soc. 143 (2) (1996) 530–543.
[39] J.R. Wilson, J.S. Cronin, A.T. Duong, S. Rukes, H.Y. Chen, K. Thornton, D.R. Mumm, S. Barnett, J. Power Sources 195 (7) (2010) 1829–1840.
[40] H. Iwai, N. Shikazono, T. Matsui, H. Teshima, M. Kishimoto, R. Kishida, D. Hayashi, K. Matsuzaki, D. Kanno, M. Saito, H. Muroyama, K. Eguchi, N. Kasagi, H. Yoshida, J. Power Sources 195 (4) (2010) 955–961.
[41] Comsol Multiphysics Version 3.4 User's Guide, 2007.
[42] M.A. Khaleel, Z. Lin, P. Singh, W. Surdoval, D. Collin, J. Power Sources 130 (1/2) (2004) 136–148.
[43] J. Deseure, Y. Bultel, L. Dessemond, E. Siebert, Electrochim. Acta 50 (10) (2005) 2037–2046.